Optimization of an optical fiber endfacet machine

Bachelorarbeit in Physik

von
Steffen Urban

angefertigt im
Institut für Angewandte Physik

vorgelegt der
Mathematisch-Naturwissenschaftlichen Fakultät
der Rheinischen Friedrich-Wilhelms-Universität
Bonn

Juni 2013

1. Gutachter: Prof. Dr. D. Meschede
2. Gutachter: Dr. F. Vewinger

Contents

1 Introduction

The interaction of light and matter is a fundamental topic in physics. In order to study this interaction optical resonators are a common used tool.
An optical resonator consist of two mirrors facing each other to confine the light to the atoms position. This results in a strong inflated electric field E inside the cavity and enhances the interaction rate g of the atom. To study this interaction processes, they need to be faster than the decay rates γ and κ. This is known as the strong coupling regime [BHW+04]:

$$g \gg \kappa, \gamma$$

The factor κ describes the losses due to the field leaking out of the cavity mirrors and can be reduced by increasing the mirror reflectivity.

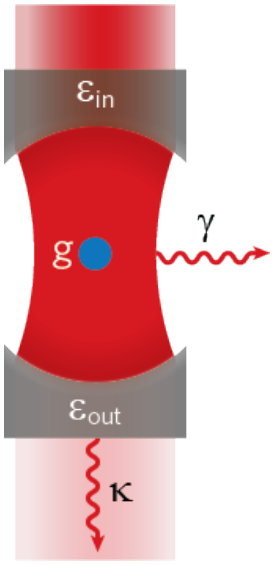

Figure 1: The interaction of an atom inside a resonant optical cavity with the lightfield is described by g,γ and κ. The factors ϵ_{in} and ϵ_{out} denote the mode-matching efficiency between fiber and cavity mode. [Fer]

On the other hand γ corresponds to the atoms spontaneous emission out of the cavity mode and is reduced for strong fields by the Purcell-Effect.
Since κ is used to gain information about the processes in the cavity, it needs to be sufficiently high:

$$g \gg \kappa \gg 1$$

As a result g needs to be increased by confining the field stronger to the atoms position. Due to the relation $g \sim E \sim \frac{1}{\sqrt{V}}$ the mode volume V of the cavity mode should be minimized. Therefore fiber cavities are used to miniaturize the whole cavity design [HSC+10]. In comparison to a conventional cavity as seen in figure 2 fiber cavities can achieve a 5 times smaller mode volume. Therefore the mirrors need to be shaped spherical to match the wavefronts of the cavity mode. Moreover fiber cavities are automatically fiber coupled which makes a efficient use of κ possible.

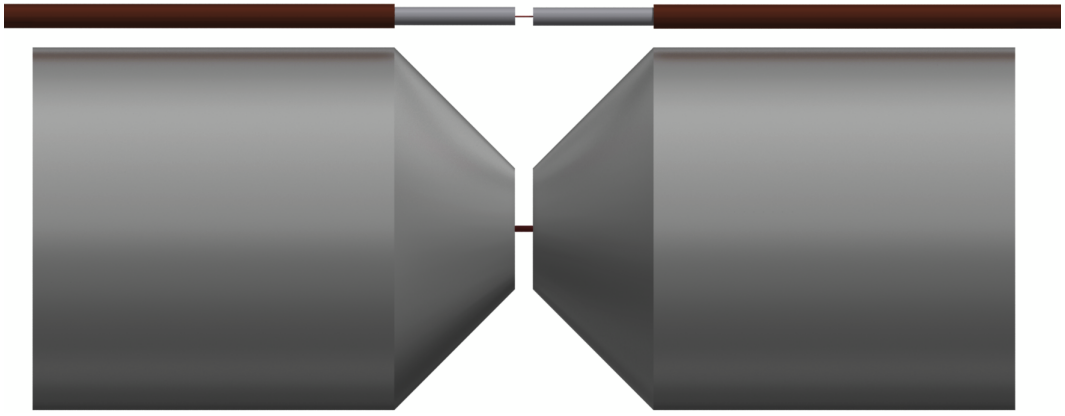

Figure 2: Comparison between a conventional optical cavity (lower picture) and a fiber cavity.

2 Endfacet machine

In order to built a fiber cavity, spherical mirrors on a fiber surface are needed. As no company provides such a product, it needs to be self made. For this the fiber surface is modified with the endfacet machine. Afterwards a high reflective dielectric coating is applied by a company.
Since the used fibers are made of silica glass, which is strongly absorbtive for radiation at 10.64 μm, a CO_2 laser is used to shape the endfacets. The idea is to ablate the material by imaging the lasers intensity profile into the cleaved fiber surface. If the laser has a Gaussian mode, the tip of the Gaussian should serve as a spherical mirror.
Therefore an endfacet machine was already built up in December 2012 [Tha12]. This thesis presents the setup status from June 2013.

2.1 Optical setup

The used CO_2 laser is a SYNRAD firestar v30 which emitts a beam with a waist of (1.25 ± 0.25) mm in CW mode [SYN]. In figure 3 the path of the laser beam is shown. As previous investigations of the laser output power stability have shown, it is better to drive the laser in a higher power regime [Tha12].

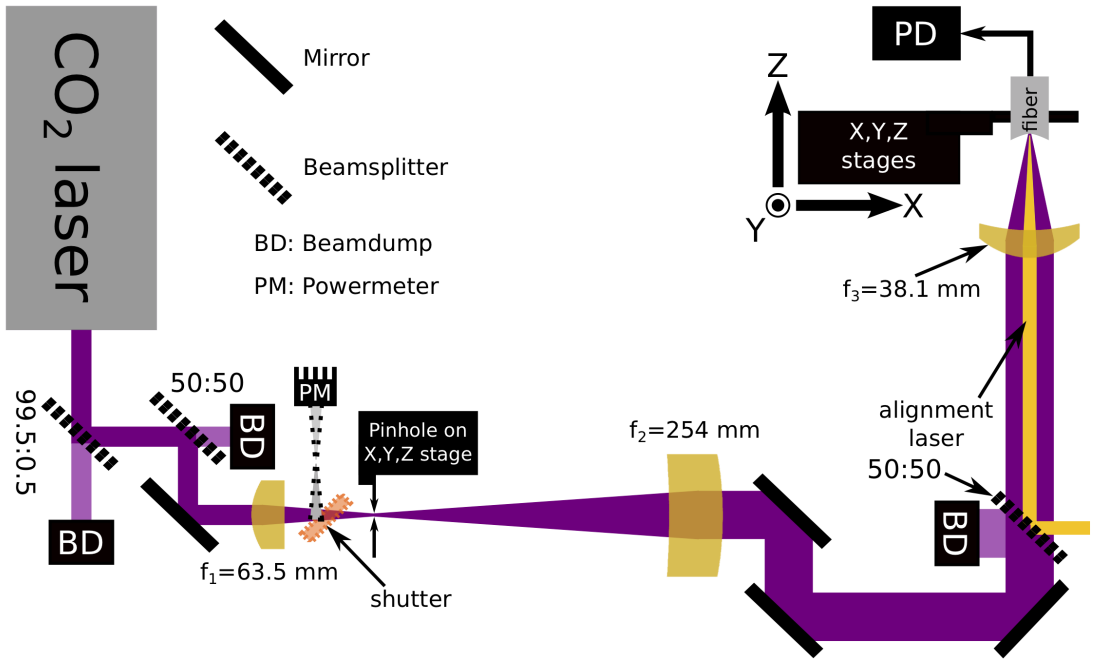

Figure 3: Fiber endfacet ablation setup: The CO_2 laser beam is magnified by a telescope (f_1 and f_2). Afterwards its focussed on the fiber (f_3). To place the fiber at the focal point of the CO_2 laser a reference laser can be overlapped to the CO_2 laser by means of a beamsplitter. When the incoupling of the reference laser into the fiber is maximized it is positioned well. The photodiode (PD) at the other end of the fiber measures the incoupling. To move the fiber it is mounted to a 3-axis stage with a precision of 0.3 μm [New].

Therefore the attenuated beam from three non polarizing beamsplitters is used. Furthermore the beam is magnified by a telescope, in order to be able to focus it down more tightly on the fiber. The telescope is build out of two Zinc Selenide (ZnSe) lenses with focal lengths of 63.5 mm and 254 mm to magnify the beam by a factor of four. A shutter, consisting of a copper total reflector, is placed near the focal point of the telescope. There the fastest shutter speed is possible, because of the small beam size. In the closed shutter position the reflected beam is used to monitor the power with a thermal powermeter (PM). Additionally a pinhole is placed at the beam waist within the telescope to clean the mode of the laser. This will be discussed in more detail in the sections 3.2 and 4. In order to obtain a surface of the laser profiles shape, the main ablation process needs to be the sublimation of the material. For this a power density bigger than 10 $\frac{\text{kW}}{\text{cm}^2}$ is necessary [SMP+03]. Given

that the beam is well collimated after the telescope (waist: w_0=5 mm and Rayleigh length: z_R=7.4 m), the meniscus lens (ZnSe, f=38.1 mm) focuses the beam down to a minimal waist of ∼26 μm and a Rayleigh range of ∼200 μm. The average power density impinging on the fiber is bigger than 24.5 $\frac{\text{kW}}{\text{cm}^2}$, since the used power on the fiber is (600-900) mW. Besides the sublimation, melting due to heating might smoothen the surface. Also floating processes of the melted glass on the surface are possible

In order to obtain different surface shapes the impinging time as well as the power of the CO_2 laser can be modified. Additionally the fiber can be placed at different z-positions relative to the focus of the CO_2 laser.

Since the time the beam impinges on the fiber has to be controlled accurately and has to be constant over the whole fiber surface, the shot is proceed as shown in figure 4 [Tha12]: Firstly an active feedback brings the power to the defined preset, secondly the laser switches off shortly when the shutter opens. While the shutter is open, the laser shoots for the given time. After this the shutter closes and the laser goes back into CW mode.

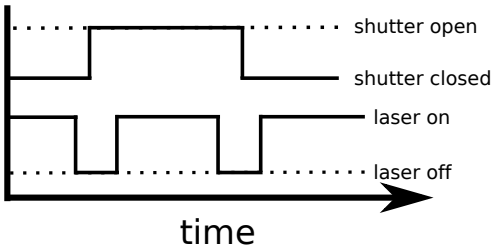

Figure 4: While the shutter moves the laser is switched off. The shot is only proceed by the laser.

2.2 Surface reconstruction

As already proposed, the mirror surfaces need to be spherical. To ensure this, a fast, precise and especially nondestructive method to obtain the fiber surface is wanted. Therefore a Michealson interferometer, shown in figure 5, is used. For the surface reconstruction the fibers can stay mounted to the stages at the shooting position. A mirror on a flip mount is used to get a look on their endfacet. As a light source a green power - LED filtered by a bandpassfilter (λ=532 nm, $\Delta\lambda$=1 nm) is used. Thus the LED's coherence length is 280 μm to get interference between the fiber surface and the reference plate, but not from other surfaces. A 50:50 beamsplitter splits the collimated incoming light to both arms. The light is focussed on the

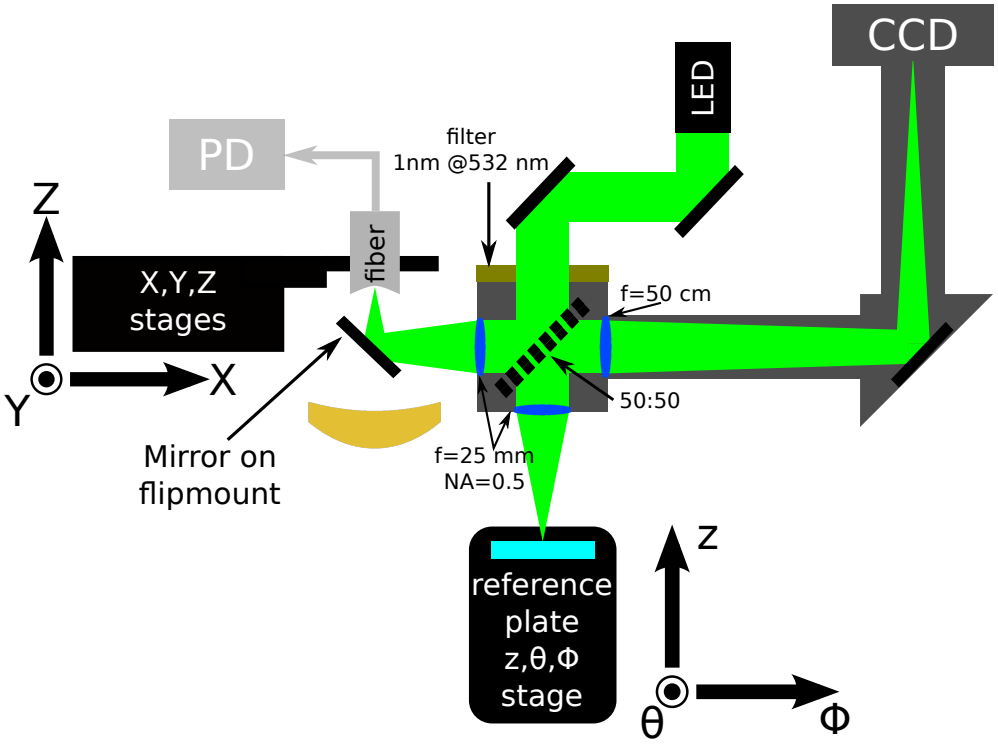

Figure 5: For the surface reconstruction a michealson interferometer is used. The surface height is measured relative to the reference plate, which is a simple glassplate. A mirror on a magnetc flipmount directly connects the interferometer to the ablation setup.

fiber and the reference plate. To collect most of the light back reflected from the curved fiber surface, lenses with a high numerical apertures are used. After recombining the beams with the beamsplitter their spatial interferogram is imaged onto a CCD camera chip. Since the reference plate is assumed to be flat, the spacial path difference between the interferometer arms should give the fiber's surface. To avoid an unnecessary tilt between the two surfaces, the reference plate can be adjusted parallel to the fiber surface by rotating it around the θ- and ϕ-axis with a mirror mount. Furthermore a micrometer stage and an additional piezo stage allow a coarse and fine tuning of the reference plate in z-direction. This ensures that both interferometer arms have the same length within the coherence length. Besides the interferometer, this configuration works as a microscope with a optical magnification of 20.

Until this step the setup already allows one to extract the fibers surface topology

from a single interferogram shown in figure 6. The intensity of the ideal interference pattern is discribed by the formula [Dem06]:

$$\mathrm{I(x,y)} = 2\mathrm{I}_0(1 - \cos(\psi(\mathrm{x,y}) + \Theta)), \quad \text{with} \quad \psi(\mathrm{x,y}) = \frac{2 \cdot 2\pi}{\lambda} \cdot \mathrm{h(x,y)}. \tag{1}$$

The phase difference between the beams reflected from the fiber and the reference plate is ψ(x,y). Θ denotes the phase difference due to a shift of the reference plate. To obtain the surface topology h(x,y), one possible way would be to determine the phase ψ(x,y) by the brightness of every pixel. Practically this would give a bad height resolution, because of potential brightness gradients and noise in the picture. Another possibility is to determine the positions of the bright and dark fringes, since the surface height difference between them is $\frac{\lambda}{4}$. Because this method would not use the full spacial resolution, a different technique called Phase-Shift-Interferometry (PSI) is used. The PSI method uses the ability of the piezo stage to shift the reference plate many times equidistant within the wavelength regime, while taking a interferogram picture at every step. These shifts are similar to an increasing phase Θ in equation 1. Figure 7A shows the brightness change of one pixel during the shifts with a fitted cosine. From independent fits

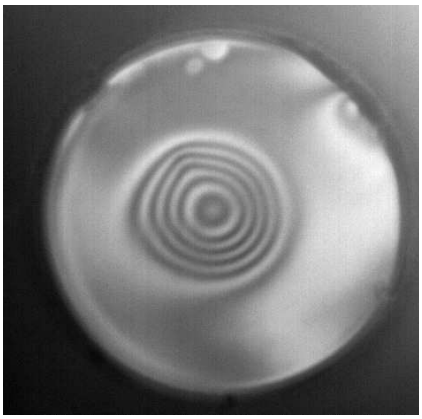

Figure 6: Single interferogram of a fiber.

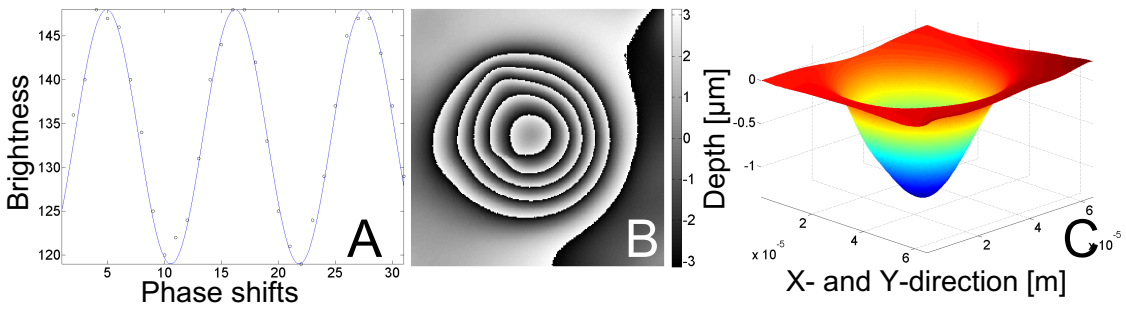

Figure 7: A: The brightness change of one pixel during the phase shifts with a fitted cosine. B: From fitting a cosine for every pixel the wrapped phasemap (from -π to π) is gained. C: By unwrapping the phase the fiber surface is obtained.

for each pixel one can determine the phase ψ(x,y) modulo 2π. The introduced setup performs 31 shifts with a stepsize of $\sim$25 nm. This turned out to be enough to fit the cosine properly. As a result the phasemap of the surface as shown in figure 7B is gained. By using a 'phase unwrapping' algorithm [Cos98] [Luo] the original phase can be reconstructed by the assumption, that the surface makes no jumps. With the help of equation 1 h(x,y) and thus the 3D surface information can be calculated. An example is given in figure 7C. The big advantages of the PSI method are the complete independence from brightness gradients, low contrast and robustness against noise in the pictures due to the fitting. Moreover the full spacial resolution is used, since the surface height is determined for every single pixel. The accuracy of the surface gained by the PSI method should be at least smaller than $\frac{\lambda}{4}$, because the observed interference pattern was stable. Vibrations in x-and y-direction should not have a big influence on the resulution, because the interferometer anyways averages over one pixel. This corresponds to 0.26 μm on the fiber. Further the optical resolution of the fiber by the lens (f=25 mm, NA=0.5) is worse than 0.7 μm, which is the overall limiting factor.

2.3 Surface analysis

In order to see how well the produced surfaces match the requirements, they need to be classified. We want to know, how elliptical the shots are and how big the curvature is. Therefore a two dimensional Gaussian is fitted to the surface, because we assumed to image a Gaussian mode into the material. Since the produced endfacets are not precisely Gaussian shaped, this function is only used to find the minor and major axis of a possible ellipticity. Afterwards the height profiles along both axes are analyzed by fitting a Gaussian and also a polynomial to the minimum of the depression. A 10th order polynomial follows the data nicely whereas it does not follow the noise. The two methods give the possibility to compare the surface to a Gaussian shape, e.g. to study reflow processes due to melting of the material. Since the surface profiles are described by analytic functions f(x), their radii of

curvature (ROC) along the profiles are given by:

$$\mathrm{ROC}(x) = \left| \frac{(1 + f'(x)^2)^{\frac{3}{2}}}{f''(x)} \right| \tag{2}$$

If one takes a closer look to the numerator of the formula, the first derivative can be an error source. Because the surface height is calculated relative to the reference plate, the surface can easily get a linear offset. Since this offset will not drop out of the ROC calculation, one has to adjust the reference plate carefully.
The future mirror surface is characterized by the minimal ROCs of the minor and major axis and their quotient (ellipticity). With this definition an ellipticity close to 0 means totally elliptical and 1 perfectly radial symmetrical. We are aiming for the latter case. Furthermore with equation 2 the size of the area with nearly constant ROC can be found

.

3 The first coating run

Before I joined the project, a set of fibers was shot with different shooting parameters. In addition the endfacets were already coated for high reflectivity (>99.9 %) at 780 nm (^{87}Rb D_2-Line) [Ste]. As shooting parameters, powers of (2.2-3) W (at the powermeter) and times of (10-40) ms were used. Additionally the fibers were placed at two different positions, 320 μm and 350 μm, relative to the CO_2 lasers focus. The used fibers were the model Cu100/110 from IVG (multi-mode) as well as the models Cu800 from IVG and SM800-125CB from Oxford electronics (both single-mode).
The idea is to characterize the endfacets using the previously introduced methods. We expect from that to learn how the different shooting parameters affect the surface. Further, flaws of the surfaces like the ellipticity and other problems in the production process can be found.

3.1 Results

As a result we obtained the characteristics of 39 fibers, when excluding problematic shots by eye. From these, 16 fibers are multi-mode and 23 are single-mode fibers (18 from IVG, 5 from Oxford electronics). In Figure 8 the center of a surface profile along an ellipticity axis can be seen. A Gaussian and a polynomial were fitted to nearly the whole surface (40 μm). From the deviation of the Gaussian to the measured points one can see that the whole surface is not Gaussian shaped. But when the fitting area is confined to the tip of the surface we observed that also the Gaussian follows the data as good as the polynomial.
The radii of curvatures of the first run were mainly between (100-400) μm which contains already the target zone ((150-180) μm) for future cavity fibers.

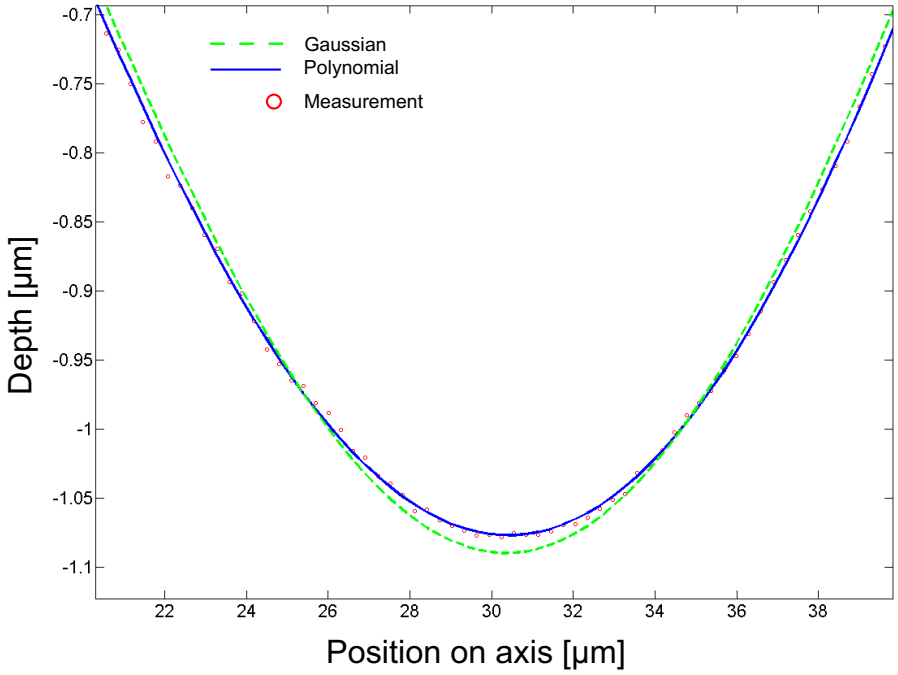

Figure 8: Height profile along one axis with fitted polynomial and Gaussian (fitting range: 40 μm). One can see the deviations of the surface tip from a perfect Gaussian.

Even the small amount of data allows one to see some systematic effects, like a decreasing ROC with an increasing power due to deeper and sharper cavities.

A histogram of the ellipticity is shown in figure 9. Due to the high amount of elliptical shots the source of the ellipticity needs to be found. Furthermore only one fiber for every shooting parameter was available after the selection. This leads to a missing statistical resolution and no statement about the reproducability of the shots can be made. Moreover the influence of the coating on the surface could not be observed since the fibers were not analyzed before the coating run.

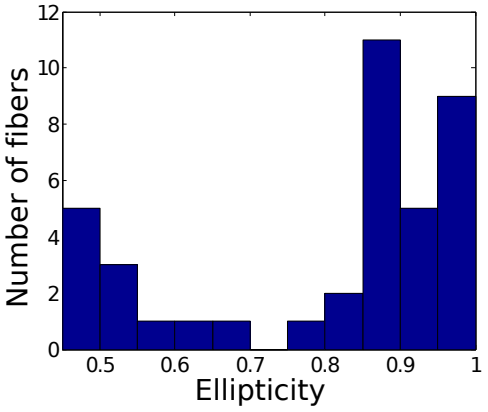

Figure 9: Histogram of the ellipticity for the first coating run. The binning size is 0.05

3.2 Technical difficulties

Laser mode

Along these observations further technical difficulties appeared. While taking shots at different positions relative to the focus, at some point, with one shot two small cavities were produced instead of one. The effect was associated with a additional higher mode to the Gaussian TEM_{00} mode. Thus an improvised pinhole (diameter: 400 μm) was placed in the telescopes focus before the first coating run to clean the mode. The pinhole should on one hand clip the power of some higher order mode. On the other hand it should increase the divergence of the transmitted part of that mode, so that it will not be focused on the fiber. At least, the phenomena could not be observed again.

To further analyze this, the laser beam was inspected before focusing down with the meniscus lens. For this the beam path was enlarged by 1.5 m and imaged on thermal paper. Figure 10 shows the transverse intensity distribution of the beam on thermal paper with and without the pinhole. The intensity distribution has in both cases no radial symmetry. Even with the pinhole the higher order mode is still visible, but seems to be more divergent. Considering the shape, we assume that the TEM_{00} mode is overlapped by a TEM_{10} mode.

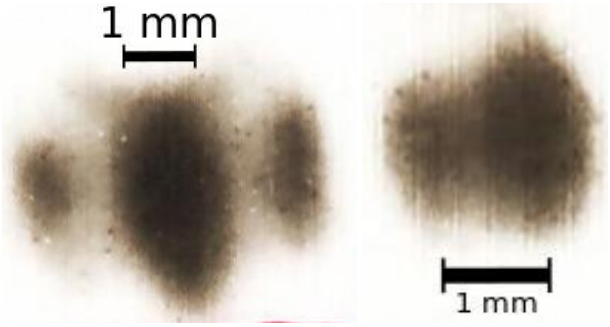

Figure 10: Mode image on thermal paper with the pinhole (left) and without the pinhole (right).

To get information about the amount of power in the higher mode, the thermal paper can not be used, because its sensitivity is nonlinear to the impinging power and it saturates quickly. This is why the power was measured at the fibers position with and without the improvised pinhole. The CO_2 lasers output power was raised from 5 % to 30 % of the maximum laser output power in steps of 0.5 %. At every power step the powermeter signal was averaged over ∼60 s to counter the power fluctuations of the laser.

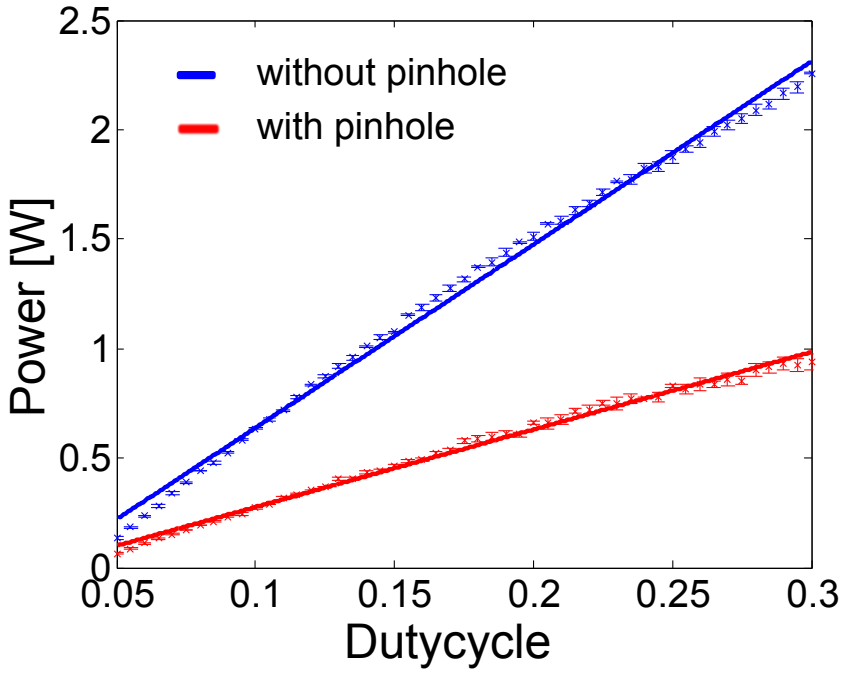

Figure 11: Averaged power at the fibers place with and without the pinhole. The strong attenuation of the beam is a clear hint to a powerful higher mode.

The obtained data is shown in figure 11, a linear regression is already done:

$$\begin{aligned} \text{without pinhole:} \quad & \text{slope} = 8.4\,\text{W} \quad \text{offset} = -0.2\,\text{W} \\ \text{with pinhole:} \quad & \text{slope} = 3.5\,\text{W} \quad \text{offset} = -0.08\,\text{W} \end{aligned}$$

When assuming that the pinhole is perfectly centered with respect to the TEM_{00} mode we would expect from the formula

$$\text{P}(\rho) = \text{P}_0 \left(1 - \exp(-\frac{2\rho^2}{\text{w}^2})\right) \quad \text{w : beamwaist at the pinhole } (108 - 173\,\mu\text{m}),$$

that a pure TEM_{00} beam looses 0.11-7 % of power due to clipping at a pinhole with radius ρ=200 μm. In contrast to that the measurement obtained an attenuation of $\sim$58 %. This attenuation is higher than expected for a TEM_{00} mode. On the one hand this can be due to a bigger waist than assumed, a decentracion of the pinhole or a powerful higher mode. Since the pinhole was aligned carefully for maximal

and symmetric transmission this should not be the case. But the attenuation is also higher than expected for a mixture of TEM_{00} and TEM_{10} modes, which might be a hint that the waist is bigger than assumed. Nevertheless a modecleaning with hard-apertures will be introduced in section 4, since the improvised pinhole had already improved the setup.
Besides a higher mode, other reasons for the observed ellipticity can be a general misalignment of the telescope or clipping at mirror edges after the telescope since the beam is very wide at this point. Therefore the telescope and the following path was realigned carefully.

Centration of the shots

Another observation is the missing centration of the shots on the fiber surface. The centration is very important, to ensure a good overlap between fiber and cavity mode. Given that the core diameter of a single mode fiber is 5 μm calculations for the overlap of the two modes require the centration to be better than 1 μm.
The current alignment method is to make some reference shot on a glassplate. Then the flipmounted mirror is placed in front of the fiber. Next the center of the shot is marked on the microscope view. Finally a prepared fiber is placed at the marked position and the mirror is taken out for the shot. Since the mirror has to be removed and replaced for every shot and the same reference shot is used multiple times, there is an increasing inaccuracy with each shot. Therefore the alignment accuracy should be increased using the reference laser and also the centration quality needs to be quantized. For this an algorithm to find the fiber center was programmed and will be presented in chapter 5.

4 Mode cleaning with hard apertures

The observed mode, consisting of a TEM_{00} mode and probably a TEM_{10} mode, has no radial symmetry. In order not to image this mode into the fiber surface, the TEM_{10} mode needs to be attenuated. Thus similar to [KAA00] we will modify the setup by adding three apertures to the telescope. This is shown in figure 12.

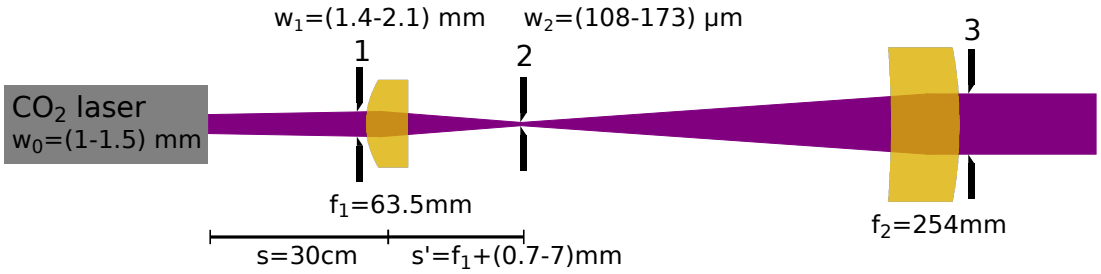

Figure 12: Propagation of the CO_2 laser beam trough the telescope. To clean the mode, aperture 1 increases the divergence of a higher mode. A pinhole (2) will clip most of the higher modes power. Aperture 3 will cut away the Airy wings from the diffraction at the pinhole.
w_X: Waist at aperture X, s': Distance between lens f_1 and w_2

The first aperture (1) increases the divergence of the higher mode compared to the Gaussian mode. Then a pinhole (2) clips as much of the higher mode as possible, but should transfer the TEM_{00} mode as good as possible. To avoid imaging the pinhole on the fiber aperture 3 will clip the Airy wings of the interference pattern from the pinhole. This means that it will only transmit the central peak of the Bessel shaped intensity distribution, which is almost Gaussian shape.
In the following the pinhole size will be calculated for an optimal supression rate of the TEM_{10} to the TEM_{00} mode. For this the properties of the propagating beam were added to figure 12 [Sel83]. Furthermore we neglect the influence of the first aperture and the diffraction at the pinhole. The intensity distribution of the TEM_{xx} is denoted by $I_{xx}(X, \phi)$, with the relative coordinate $X=\frac{r}{w_2}$. The pinhole radius is ρ. Then the normalized power transmittion rate through a pinhole with

the truncation ratio Y=$\frac{\rho}{w_2}$ reads:

$$T_{xx} = \frac{\int_0^{2\pi}\int_0^{Y} I_{xx}(X,\phi)\cdot X \, dXd\phi}{\int_0^{2\pi}\int_0^{\infty} I_{xx}(X,\phi)\cdot X \, dXd\phi}$$

Since we are interested in the case $T_{00}>T_{10}$, figure 13 shows T_{00}-T_{10} for the Hermite-Gauss modes TEM_{00} and TEM_{10} [Mes08].

The maximum point at Y=$\frac{1}{\sqrt{2}}$ indicates the optimum pinhole size. For our not precisely known beam this leads to the range of approximately (152-245) μm for the pinhole diameter. Since we are expecting an improvement of the divergence of the two modes from aperture 1, pinholes with a diameter between (210-310) μm were ordered. The size of aperture 1 and 3 as well as the optimal pinhole size will be figured out experimentally.

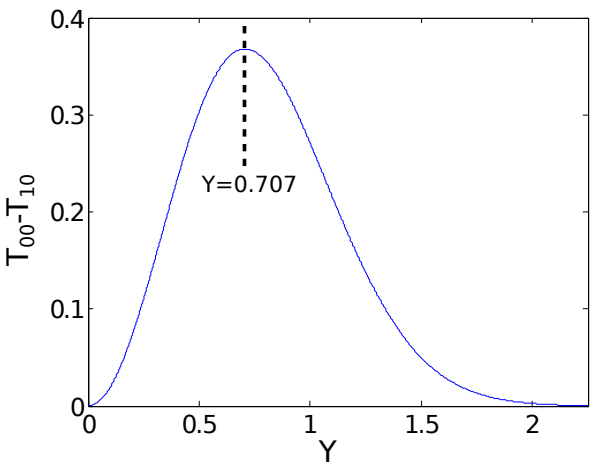

Figure 13: Variation of T_{00}-T_{10} as a function of the beam truncation ratio Y.

To compare the theoretical optimal pinhole size with the build in improvised pinhole the rate of T_{00} and T_{10} shows:

$$\text{improvised pinhole: } \frac{T_{00}}{T_{10}} = 1.46 - 1.24$$

$$\text{optimal pinhole: } \frac{T_{00}}{T_{10}} = 2.4$$

One can see, that the suggested pinhole will lead to a much stronger suppression of the TEM_{10} mode compared to the TEM_{00} mode. With this we are looking forward to improve the ellipticity significant.

5 Fiber edge recognition algorithm

In order to obtain a quantized statement about the centration quality of the shots, an algorithm to find the fiber center will be presented. This will enable one to calculate the distance of the depressions center to this point. As a source for the algorithm the interferograms from the PSI method are used. Since a single interferogram contains a lot of disturbing fringes on the fibers surface, the average over all interferograms is taken. This looks like a microscope picture and can be seen in figure 14A. Because the fiber surface itself contains no trace for its center, the fibers outer edge needs to be found. As seen in the picture, the fiber edge has a strong contrast. Therefore the sum of the absolute gradients in both spacial directions is high at the fibers edge. In picture 14B an example is shown.

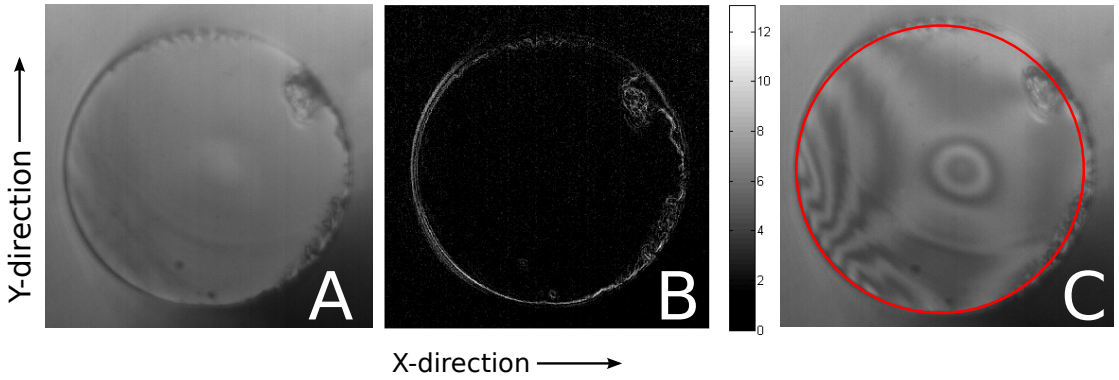

Figure 14: A: Average picture over all PSI interferograms. B: Sum of gradients in x- and y-direction of picture A. C: On high gradient points fitted circle matches nearly the fiber edge

With a predefined threshold one can find the points lying on the fibers edge and avoid the background noise. Considering that the view is orthogonal to the fibers surface, the edge of the fiber should be a perfect circle. This is why a circle can be fitted to the extracted points. Figure 14C shows the result of this method. Due to imperfections of the fiber edge or dust on the fiber the fit does not work out well. This is a result of the leastsquares fitting method, which trys to minimize the distance of the circle to every point, even if its caused by a defect. To avoid this, the circle is approximated using the cross correlation. For this, we consider two

matrices A and B which are the same size as the fibers picture. Every matrix entry corresponds to one pixel. Further matrix A contains the points on the fiber edge as entries which are 1 while all other entries are zero. The second matrix B contains a ring of ones that has the diameter of the fiber and is placed at a well known position of the matrix. Now we imagine the matrix B on top of matrix A. The correlation of the two matrices is the sum of the product of all matrix elements that are lying on top of each other. For the cross correlation the correlation of the two matrices will be calculated for every relative position (x_{off},y_{off}) of them to each other [Wer11]:

$$\text{Xcorr} = (\text{A} * \text{B})(x_{off}, y_{off}) = \sum_{x} \sum_{y} \text{A}(x,y) \cdot \text{B}(x+x_{off}, y+y_{off})$$

Since this is similar to a convolution, the cross correlation can be calculated as:

$$(\text{A} * \text{B})(x,y) = \mathcal{F}^{-1}\left((\mathcal{F}(A) \cdot \mathcal{F}(B)\right)$$

With the help of fast Fourier transform algorithms (FFT) the cross calculation can be calculated very efficient. When the cross correlation is maximized, the best match between A and B is achieved. The result of the cross correlation is in this case the number of matching points. Figure 15 shows the approximated circle using the cross correlation method. The advantage of this method is that it tries to exactly match as many point as possible with the predefined pattern and not to get only close to all of them.

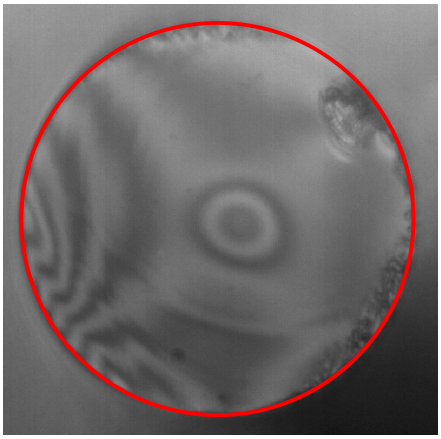

Figure 15: Approximated circle using the cross correlation.

But still the circle matches the fiber only within $\sim$(2-5) μm. This uncertainty seems to be caused by slightly differing fiber sizes and a tilted look on the endfacets. Also the averaging over all interferograms blurs the edge of the fiber. Therefore in the future a better trace for the fiber center might be the from the other end of the fiber enlightened core of the fiber.

6 Reference laser

As already mentioned before, the used method to align the fibers to the focus of the CO_2 laser is not very reliable. Hence the alignment should be done with an reference laser setup as seen in figure 16. The reference laser is overlapped on a long path to the CO_2 laser beam. Therefore we know, that when the fiber is aligned to the reference laser, it is also aligned to the CO_2 laser. When the incoupling of the reference laser into the fiber is maximized, the fiber is aligned to both, CO_2 and reference laser. For this the fiber is moved with the stages in the x- and y-direction while measuring the incoupled power with a photodiode at the other end of the fiber. This will only work if the laser is power stable. Additionally it should ideally have a wavelength close to 10.6 μm to avoid chromatic aberrations at the meniscus lens. At a previous stage of the setup a 1550 nm laserdiode was used as a reference laser, but it seemed not to be power stable enough. Therefore it was replaced by a stabilized 852 nm diode laser. When testing the setup, the CO_2 laser shots were $\sim$70 μm away from the fiber center. The reason for this is probably the chromatic aberration of the meniscus lens. To check this, table 1 shows the results of an OSLO® ray tracing simulation. When

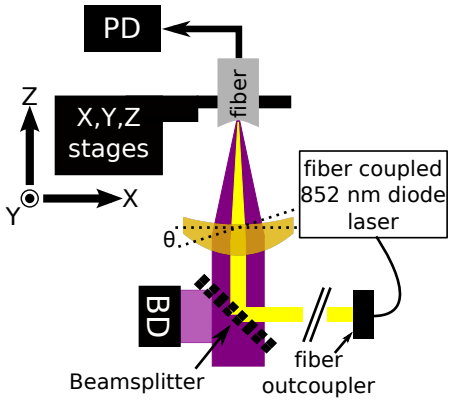

Figure 16: Reference laser setup using a 852 nm diode laser. CO_2 laser and reference laser are overlapped by a beamsplitter. The into the fiber coupled power of the reference laser can be measured with the photodiode (PD).

wavelength λ	10.6 μm	1550 nm	852 nm
n_λ [Ref]	2.403	2.456	2.512
f_{men} (OSLO®)	35.87 mm	34.6 mm	33.15 mm
d_λ for Θ=1° (OSLO®)	0.67 mm	0.647 mm	0.622 mm

Table 1: Due to the big changes of the refractive index n_λ of ZnSe also the focal length f_{men} of the meniscus lens changes a lot. The distance of the focus point from the lenses optical axis, when the lens has a tilt of Θ=1° with respect to the beams, is denoted by d_λ.

assuming a tilt of the lens (Θ=1 °) the focal points of the beams differ lateral by several tens μm from each other. Since the aim for the alignment quality is ~1 μm we checked how precise the alignment can be and if it is worth to continue with the reference laser.

Therefore the incoupled power of the 852 nm laser was measured while moving a single-mode fiber (Thorlabs SM800-5.6-125) with the stages in x- and y-direction. A 20x20μm grid was scanned in 1 μm steps. Furthermore the scan was done at the focus of the CO_2 laser and also in the focus of the reference laser. The beam of the diode laser was made divergent with the fiber outcoupler to minimize the distance from the reference lasers focus to the focus of the CO_2 laser beam. After that the focal points differ by ~300 μm. To compensate fast power oscillations, the signal was averaged over 250 ms with 10 measurements. Figure 17 shows the results. The data is interpolated linear. In picture A one can see that the incoupling is con-

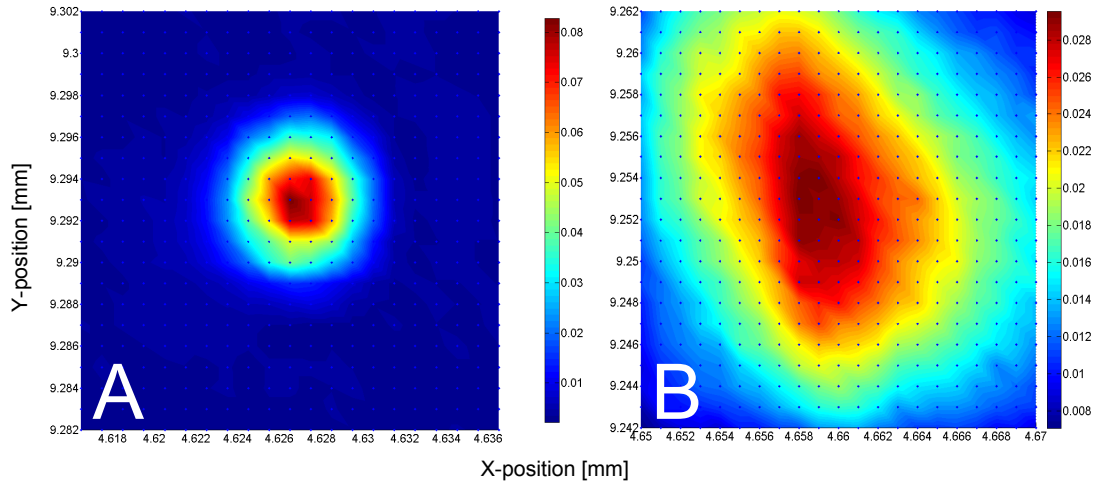

Figure 17: Picture A shows the incoupling signal of a single-mode fiber at the focus of the reference laser. In picture B the same measurement is done in the focal plane of the CO_2 laser.

fined to ~6x6 μm. The maximum point might be easily determined within 1 μm. Moreover the signal inhibits a rotation symmetry. Picture B contains not the full incoupling range, but one can already see a worse symmetry and signal to noise ratio. The missing symmetry can be due to a not perfectly aligned meniscus lens. Both pictures show, that the intensity distribution of the reference laser is small compared to the fiber surface. Thus it can only be used for the fine alignment.

For a multimode fiber, this would probably mean, that the alignment needs to be done even further out of the diode lasers focus.
To sum up, the reference laser can achieve the required precision. In order to avoid the effects of the chromatic aberration, one could place the lens more accurately, e.g. relative to the diode laser with a beam profile camera. Or one could use a concave mirror instead of the lens which has no chromatic aberration.

7 Conclusion and Outlook

To conclude, in the framework of this thesis we analyzed the first with the endfacet machine produced fiber mirrors. For this the analysis structure was tested and worked out. This gives the possibility to study produced fiber surfaces in more detail. For example reflow processes might be characterized and even used for better endfacet shapes. In addition, the measured 3D surfaces can be used to simulate parameters of cavities built from the fibers and compare them to measured cavity parameters. Furthermore the possibility to select fibers before the next coating run is enhanced and strongly recommended.
We analyzed the problems regarding the laser mode and the centration of the shots. In the next steps of the setup the modecleaning with three hard-apertures will be applied to clean the mode and reduce the ellipticity. Moreover the fiber edge recognition algorithm gives the possibility to quantize different alignment techniques as well as to make a post selection of already shot fibers. With the scan method described in chapter 6 the reference laser profile can be observed after the meniscus lens. Furthermore it can be used to align the reference laser behind the meniscus lens to the CO_2 laser.
The next overall aim of the project is to get the setup ready for a next coating run, in order to build the cavity. For this the most important step is to get information about the reproducability of the shots. Therfore one needs to make a high number of shots on fibers or at least on silica glassplates.

References

[BHW+04] Alexandre Blais, Ren-Shou Huang, Andreas Wallraff, S. M. Girvin, and R. J. Schoelkopf. Cavity quantum electrodynamics for superconducting electrical circuits: An architecture for quantum computation. Phys. Rev. A, 69:062320, Jun 2004.

[Cos98] M. Costantini. A novel phase unwrapping method based on network programming. Geoscience and Remote Sensing, 36(3):813–821, 1998.

[Dem06] W. Demtröder. Experimentalphysik 2: Elektrizität und Optik. Springer, 2006.

[Fer] Jose C. Gallego Fernández.

[HSC+10] D Hunger, T Steinmetz, Y Colombe, C Deutsch, T W Hänsch, and J Reichel. A fiber fabry–perot cavity with high finesse. New Journal of Physics, 12(6):065038, 2010.

[KAA00] F.Sanchez & M. Brunel K. Ait-Ameur. The transfer of TEM_{00} and TEM_{01} beams through a hard-aperture. Journal of Modern Optics, 47(7):1203–1211, 2000.

[Luo] Bruno Luong. Constantini phase unwrapping.

[Mes08] D. Meschede. Optik, Licht und Laser. Vieweg+Teubner, 2008.

[New] Newport. MFA Series - Miniature Linear Stages.

[Ref] RefractiveIndex.info. Refractive index database.

[Sel83] Sidney A. Self. Focusing of spherical Gaussian beams. Applied Optics, 22(5):658–661, 1983.

[SMP+03] V.K. Sysoev, V.I. Masychev, B.P. Papchenko, S.Ya. Rusanov, A.A. Yakovlev, and N.P. Glukhoedov. High-Rate IR Laser Evaporation of Silica Glass. Inorganic Materials, 39(5):532–537, 2003.

[Ste] Daniel A. Steck. Rubidium 87 D Line Data, available online at http://steck.us/alkalidata (revision 2.01, 2 May 2008).

[SYN] SYNRAD. firestar vSeries, 30 & 40W CO_2 lasers.

[Tha12] Natalie Thau. Optical fiber cavities, 2012.

[Wer11] Dirk Werner. Funktionalanalysis. Springer, 2011.

Erklärung zur selbstständigen Anfertigung

Ich versichere, dass ich diese Arbeit selbstständig verfasst und keine anderen als die angegebenen Quellen und Hilfsmittel benutzt sowie die Zitate kenntlich gemacht habe.

Ort, Datum

Steffen Urban